

Journal Pre-proof

Interplay between oxygen doping and ultra-microporosity improves the CO₂/N₂ separation performance of carbons derived from aromatic polycarboxylates

Saeed Khodabakhshi, Marco Taddei, Jennifer Rudd, Matthew J. McPherson, Yubiao Niu, Richard E. Palmer, Andrew R. Barron, Enrico Andreoli

PII: S0008-6223(20)31159-3

DOI: <https://doi.org/10.1016/j.carbon.2020.11.080>

Reference: CARBON 15893

To appear in: *Carbon*

Received Date: 9 September 2020

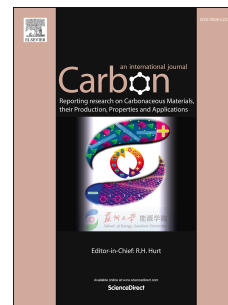
Revised Date: 17 November 2020

Accepted Date: 27 November 2020

Please cite this article as: S. Khodabakhshi, M. Taddei, J. Rudd, M.J. McPherson, Y. Niu, R.E. Palmer, A.R. Barron, E. Andreoli, Interplay between oxygen doping and ultra-microporosity improves the CO₂/N₂ separation performance of carbons derived from aromatic polycarboxylates, *Carbon*, <https://doi.org/10.1016/j.carbon.2020.11.080>.

This is a PDF file of an article that has undergone enhancements after acceptance, such as the addition of a cover page and metadata, and formatting for readability, but it is not yet the definitive version of record. This version will undergo additional copyediting, typesetting and review before it is published in its final form, but we are providing this version to give early visibility of the article. Please note that, during the production process, errors may be discovered which could affect the content, and all legal disclaimers that apply to the journal pertain.

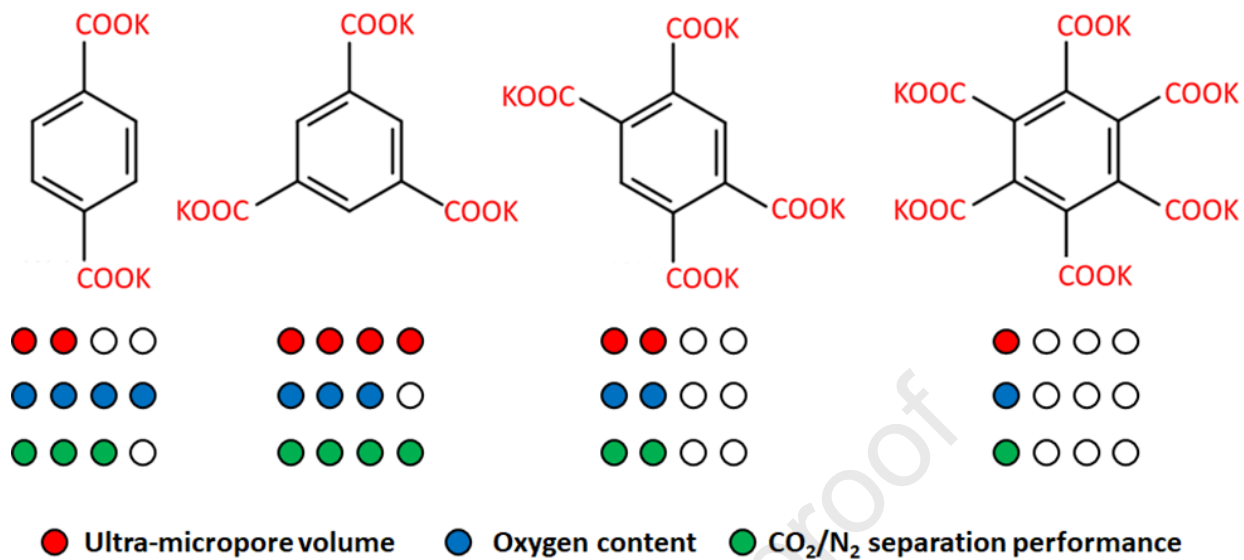
© 2020 Published by Elsevier Ltd.



CRedit Author Statement

Saeed Khodabakhshi: Conceptualization, Methodology, Formal Analysis, Investigation, Writing - Original Draft, Writing - Review & Editing, Funding Acquisition **Marco Taddei:** Conceptualization, Methodology, Formal Analysis, Investigation, Writing - Original Draft, Writing - Review & Editing, Visualization, Funding Acquisition **Jennifer Rudd:** Methodology, Formal Analysis, Investigation, Writing - Original Draft **Matthew J. McPherson:** Investigation **Yubiao Niu:** Investigation **Richard E. Palmer:** Supervision, Funding Acquisition **Andrew R. Barron:** Supervision, Funding Acquisition **Enrico Andreoli:** Supervision, Writing - Review & Editing, Funding Acquisition

Porous carbons from pyrolysis of aromatic polycarboxylate precursors



Interplay between oxygen doping and ultra-microporosity improves the CO₂/N₂ separation performance of carbons derived from aromatic polycarboxylates

Saeed Khodabakhshi,^{a,*†} Marco Taddei,^{a,b,*†} Jennifer Rudd,^a Matthew J. McPherson,^a Yubiao Niu,^c Richard E. Palmer,^c Andrew R. Barron,^{a,d,e} Enrico Andreoli^{a,*}

^aEnergy Safety Research Institute, College of Engineering, Swansea University, Bay Campus, Swansea SA1 8EN, UK. Email: saeid.khodabakhshi@swansea.ac.uk; e.andreoli@swansea.ac.uk

^bDepartment of Chemistry and Industrial Chemistry, University of Pisa, Via Giuseppe Moruzzi 13, 56124 Pisa, Italy. Email: marco.taddei@unipi.it

^cCollege of Engineering, Swansea University, Bay Campus, Swansea, SA1 8EN, UK

^dDepartment of Chemistry, Rice University, Houston, Texas 77005, USA

^eFaculty of Engineering, Universiti Teknologi Brunei, BE1410, Brunei Darussalam

[†]These authors contributed equally

Abstract

Microporous carbons were prepared starting from a series of benzene polycarboxylic acids following two strategies: (i) activation- and template-free pyrolysis and (ii) ion-exchange pyrolysis. The proposed synthetic strategies are facile approaches to produce highly microporous carbons that avoid the use of large amounts of corrosive and expensive chemical activators or templates. By varying the number of carboxylic acid groups, the charge balancing species and the degree of deprotonation of the precursors, microporous carbons with diverse morphologies, textural properties and oxygen contents were obtained and their CO₂ and N₂ sorption properties were assessed. The abundant micropores made the materials suitable for CO₂ adsorption at low pressure and ambient temperature, achieving CO₂ uptake as high as 4.4 mmol/g at 25 °C and 1 bar, competitive with those reported for porous carbons produced using large excess of alkali metal based activating agents. It was found that high performance, in terms of CO₂ uptake and CO₂/N₂ selectivity, was linked to the simultaneous presence of large ultra-micropore volume and high oxygen content in the sorbents. This suggests that the interplay of ultra-microporosity and oxygen doping matters more than the two features taken singularly in determining the CO₂/N₂ separation properties of porous carbons at low pressure.

KEYWORDS: Porous carbons; carbon capture; ultra-microporosity; oxygen doping

Journal Pre-proof

Introduction

Inorganic [1, 2], organic [3-5], polymeric [6], and hybrid inorganic–organic[7-10] porous materials play a key role in many technologies including water treatment, gas capture and separation, supercapacitors, catalysis, sensors, tissue engineering, drug delivery, and photonics [11, 12]. The pore walls of porous materials can interact with atoms, ions, and molecules, or load and hold solid particles, liquids, and gases [13-15]. Among various porous materials, porous carbons (PCs), also known as activated carbons, have been vastly utilised as liquid and gas adsorbents because of their high surface area, tuneable pore size distribution, notable stability against high temperature and humidity, good adsorption kinetics, sustainability, and cheapness [5, 16-18]. In addition, in order to achieve suitable properties for specific applications [19-22], heteroatoms can be incorporated into the carbon framework, either on the carbon surface or as a part of the covalent network [23-26].

The extensive and continued use of fossil fuels has led to the fast and large accumulation of carbon dioxide (CO₂), sulphur dioxide (SO₂), and nitric oxide (NO), and soot particles in the atmosphere [27]. Concern over CO₂ emissions, which are the main cause of global warming and climate change, has been growing restlessly in recent years. CO₂ capture is regarded as an effective measure to mitigate climate change, even though challenges still remain to be addressed, such as high production and regeneration cost of the sorbent material [28, 29]. Among various materials developed for post-combustion CO₂ capture, PCs have been known as promising candidates due to possessing ideal properties and presenting high adsorption capacity and easy regeneration at ambient temperature [30]. There are a number of contributing factors influencing the gas uptake in porous materials including surface area, pore volume and size, doping and even morphology of the adsorbent [31-35]. It is widely agreed that, at atmospheric pressure, CO₂, with a kinetic diameter of 3.3 Å, tends to be accommodated in micropores smaller than 10 Å [36]. It has indeed been found that microporous structures are more favourable for CO₂ uptake at low pressure (below 1 bar), while mesoporous structures have higher capture performance at pressure higher than 1 bar [37, 38]. In other words, lower pressures demand narrower pores for adsorption [39]. In this regard, a great deal of effort has been devoted to tailoring PCs for desired applications mainly based on the use of activating agents such as alkali-metal ions; however, carbon source and activator can be crucial factors affecting the pore volume and size.

There still exist controversial opinions as to whether the textural properties are dominant over surface chemistry in PCs to control CO₂ capture efficiency at different pressures. Note that we use the term “surface” herein to indicate the guest-accessible surface,

whereas we use “external surface” when referring to the portion of sample probed by X-ray photoelectron spectroscopy (XPS). A classic example is whether the capture performance of oxygen-doped PCs is mostly dominated by the oxygen content or by the pore structure of the sorbent. Oxygen doped porous carbons made from oxygen-rich polymer precursors have been employed to show the significant impact of oxygen on increasing CO₂ uptake performance, especially at high pressure [40]. It also has been suggested that the surface chemistry, rather than the textural properties, governs the CO₂ capture performance at lower pressures, while the textural properties become more important at higher CO₂ pressures, when the adsorption process becomes controlled by the micropore filling mechanism [41, 42]. Carboxyls and hydroxyls have been suggested as the most effective oxygenated functionalities for selective adsorption of CO₂, due to their high polarity, compared to carbonyls and ethers [43, 44]. A recent work reported that oxygen can actually be detrimental to the capture performance, although in this case the focus was on the external surface functionalisation [45]. In the same work, it was suggested that, at lower temperatures (0 °C), the effect of textural properties is dominant over surface chemistry and that the ultra-micropore volume alone determines the adsorption behaviour. Some authors have recently proposed that both textural properties and oxygen content contribute together to determine the adsorption behaviour of the sorbent [46, 47].

In this study, we used aromatic carboxylic acids as precursors to prepare microporous carbons with morphology and textural properties influenced by both the number of carboxylic acid groups in the precursor and the activation conditions. In particular, we investigated a range of benzene polycarboxylic acids (BCAs), namely, terephthalic acid (H2-TP), trimesic acid (H3-TM), pyromellitic acid (H4-PM) and mellitic acid (H6-M) (Fig. 1), for the production of oxygen-doped PCs. We chose these BCAs since they have the same central phenyl core but increasing numbers of carboxylic groups and can be good model compounds to identify trends in textural properties, surface chemistry, and gas separation performance. The resulting PCs were fully characterised using electron microscopy, CHN elemental analysis, XPS and gas sorption analysis, and the CO₂ capture performance was correlated to their composition and porous features. The proposed approach could be considered to produce cheap porous carbon from oxy-cracked petroleum coke, a byproduct of oil refinery, rich in carboxyl groups [48].

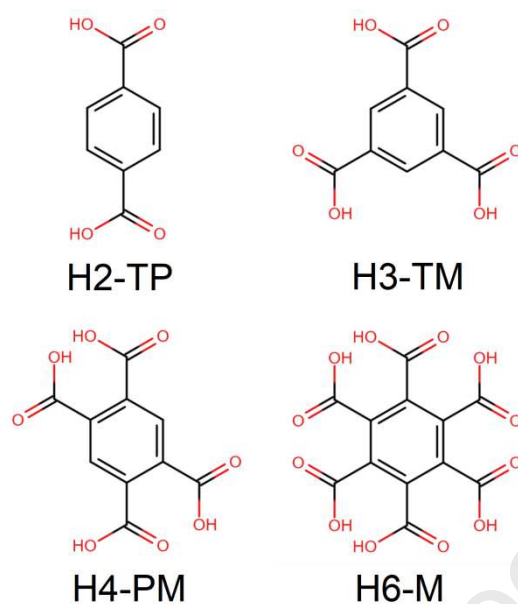


Fig. 1. Benzene polycarboxylic acids used in this study as precursors of microporous carbons.

Experimental section

Materials

All chemicals were purchased from Sigma-Aldrich and used without further purification.

Synthesis

Products P-H3-TM and P-H6-M were obtained by direct pyrolysis of H3-TM and H6-M, respectively, without any pre-treatment in a cylindrical furnace at 800 °C under Ar for 1 h with a heating rate of 1 °C/s.

The process for PCs obtained from ion-exchanged BCAs is as follows: the BCA precursors were added into the aqueous MOH (where M = K, Na) solution with the following MOH/BCA ratios: KOH/H2-TP 2:1, KOH/H3-TM 3:1, NaOH/H3-TM 3:1, KOH/H4-PM 4:1, KOH/H6-M 6:1, KOH/H6-M 3:1. The mixture was stirred at 70 °C for 3 h, followed by water evaporation under reduced pressure. The ion-exchanged products were dried in an oven at 90 °C for 4 h prior to carbonisation. Then, the sample was put in a ceramic boat in the cylindrical tube followed by thermal treatment under argon at 800 °C for 1 h with a heating rate of 1 °C s⁻¹. The resulting sample was washed with deionised H₂O and then immersed in HCl solution (0.1 N) under stirring for 15 min. After that, the sample was thoroughly washed with deionised H₂O until neutral pH was achieved. The final PCs were obtained after drying in a vacuum oven at 80 °C overnight.

Characterisation

Scanning Transmission Electron Microscopy (STEM) and Transmission Electron Microscopy (TEM) were performed with a Thermo Fisher Scientific Talos F200X at 200 kV. The STEM was conducted with a convergence angle of 20 mrad and a high angle annular dark field (HAADF) detector operating with inner and outer angles of 62 mrad and 164 mrad. SEM images of the PCs were obtained with a JEOL 7800F FEG SEM (JEOL, Akishima, Tokyo, Japan). The Raman data of the PCs were recorded at room temperature using a Renishaw inVia Raman Microscope (Renishaw plc, Misken, Pontyclun, UK) with excitation wavelength of 633 nm. The elemental analyser (Vario EL cubewas, Germany) was used to determine the amount of carbon, hydrogen and oxygen.

XPS was performed using a Kratos Axis Supra (Kratos Analytical, Japan) utilising a monochromatic Al-K α X-ray source (K α 1486.58 eV), 15 mA emission current, magnetic hybrid lens, and slot aperture. Region scans were performed using a pass energy of 40 eV and step size of 0.1 eV. Peak fitting of the narrow region spectra was performed using a Shirley type background, and the synthetic peaks were of a mixed Gaussian-Lorentzian type. Carbon sp^2 was used for charge referencing with the binding energy of the sp^2 carbon set to 284.0 eV.

N₂ adsorption/desorption isotherms at 77 K and CO₂ adsorption isotherms at 273 K were obtained using a Quantachrome Nova 2000E (Quantachrome Instruments, Boynton Beach, FL, USA). About 50-100 mg of sample was used. The samples were degassed at 150 °C for 4 h under dynamic vacuum prior to analysis. Specific surface areas were determined by applying the Brunauer–Emmett–Teller (BET) method to the N₂ isotherms. The BET equation was fitted in the following P/P₀ ranges: P-K2-TP: 0.002-0.032; P-K3-TM: 0.0028-0.045; P-K4-PM: 0.003-0.043; P-K6-M: 0.0013-0.081; P-H3-TM: 0.002-0.03; P-Na3-TM: 0.006-0.034; P-H3K3-M: 0.005-0.064; P-H6-M: 0.0026-0.043. Total pore volume was measured at P/P₀ of 0.9 in the N₂ isotherms. Micropore volume was determined using the t-plot method (Carbon Black equation) applied in the 0.2 - 0.45 P/P₀ range of the N₂ isotherms. Pore size distribution in the range of pore width >6 Å was determined applying the Equilibrium model within the Quenched solid Density Functional Theory (QSDFT) method to the N₂ isotherms, assuming slit-shaped pores. Pore size distribution in the range of pore width <15 Å was determined applying the Non-Linear Density Functional Theory (NLDFT) method to the CO₂ isotherms.

High pressure CO₂ and N₂ adsorption isotherms up to 10 bar were measured with a Quantachrome iSorb High Pressure Gas Analyser (Germany) at 25 °C, 35 °C and 45 °C for CO₂ and at 25 °C for N₂. About 200 mg of sample was used for the adsorption studies. All

the samples were degassed at 160 °C under dynamic vacuum for 2 h prior to analysis. Degasification temperature was internally controlled by covering the cell containing sample with a thermal jacket, while the adsorption temperature was adjusted by a jacketed beaker connected to a circulating bath containing a water/ethylene glycol mixture. The CO₂ adsorption isotherms were fitted with the Dual-Site Langmuir model:

$$n = q_1 \cdot \frac{k_1 \cdot P}{1 + k_1 \cdot P} + q_2 \cdot \frac{k_2 \cdot P}{1 + k_2 \cdot P}$$

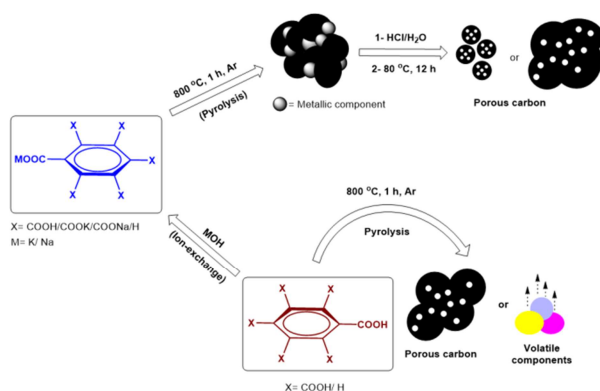
The CO₂ isotherms were also fitted with the Virial equation, using six common parameters ($a_0, a_1, a_2, a_3, a_4, a_5, b_0$) for three isotherms:

$$\ln P = \ln n + \frac{1}{T} \sum_{i=0}^5 a_i n^i + b_0$$

The N₂ adsorption isotherms were fitted with the Langmuir model. Isothermic heats of CO₂ adsorption (Q_{st}) were calculated in two ways: I. using the Clausius-Clapeyron equation, from the isotherms collected at 25, 35 and 45 °C and fitted with the Dual Site Langmuir model; II. using the five temperature dependent parameters used to fit the Virial equation ($a_0, a_1, a_2, a_3, a_4, a_5$). Ideal adsorbed solution theory (IAST) selectivity for a 0.15:0.85 CO₂/N₂ mixture at 25 °C in the 1-10 bar pressure range was calculated using the software *IAST++* [49].

Results and Discussion

Scheme 1 represents pathways to produce oxygen doped porous carbon from BCAs as carbon and oxygen source, either in protonated form or when neutralised with NaOH or KOH. We note that the hydroxide activating agent is here used in strictly stoichiometric amounts, in order to avoid the drawbacks associated with usage of large excess of activating agents, such as corrosion, low yield and environmental hazard [30]. Successful direct pyrolysis was only observed for H3-TM and H6-M, whereas H2-TP and H4-PM sublimed before being carbonised. The yield of PCs derived from pyrolysis of H3-TM and H6-M (~25-30%) was lower than those derived from their ion-exchanged counterparts (45-55%), suggesting that aromatic salts benefit from higher stability and undergo less burn-off.



Scheme 1. Reaction Scheme for the PCs synthesis using benzene polycarboxylic acid precursors.

We prepared and characterised a total of eight samples. For the sake of clarity, we have separated them into the following three series, which will be discussed separately in order to identify dependence on one parameter at the time: 1) Effect of the number of carboxylic groups on the aromatic ring of BCAs – i.e. two, three, four, six – when fully neutralised with KOH. These samples are named P-K2-TP, P-K3-TM, P-K4-PM, P-K6-M, respectively. 2) Effect of the nature of the charge balancing species – i.e. H, Na, K – in TM. These samples are named P-H3-TM, P-Na3-TM and P-K3-TM, respectively. 3) Effect of the degree of deprotonation in M – i.e. zero, three, six - when neutralised with KOH. These samples are named P-H6-M, P-H3K3-M, P-K6-M, respectively.

Effect of the number of carboxylic acids

We started our investigation by preparing a series of samples, derived from commercially available BCA precursors, with varying number of carboxylate groups. The effect of number of COOK groups on the morphology of the resulting PCs was investigated by SEM, TEM and STEM. SEM images (Fig. S1, see Supporting Information, SI) for products shows an agglomeration of carbon particles forming different shapes, evident at high magnification. Using STEM and TEM, a better picture of the surface morphology was gathered, see Fig. 1 and Fig. S2 (SI). As can be seen from Fig. 1, a similar spherical shape in range of 50-200 nm is observed for P-K3-TM and P-K6-M, with plenty of pores especially visible in the former. P-K2-TP displayed ill-defined shape and P-K4-PM showed sheet-like morphology with evidence of pores with size of about 50 nm.

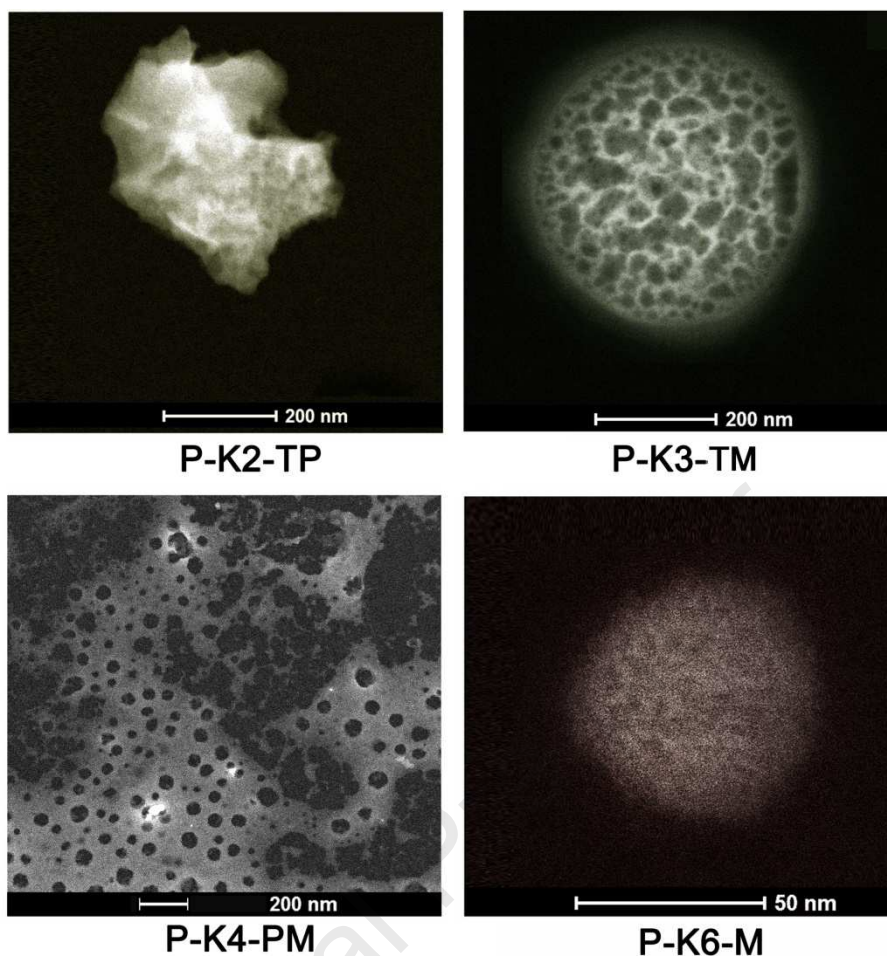

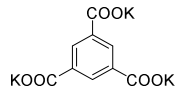
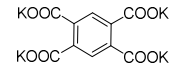
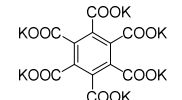


Fig. 1 STEM images of P-K2-TP (top left panel), P-K3-TM (top right panel), P-K4-PM (bottom left panel) and P-K6-M (bottom right panel).

CHN elemental analysis shows that the oxygen content found in the pyrolysed product is inversely proportional to that of the BCA precursor, increasing in the order P-K6-M < P-K4-PM < P-K3-TM < P-K2-TP (Table 1). The observed inverse trend of the oxygen content between salt precursors and obtained PCs is likely because the presence of more oxygen in precursor demands more MOH in stoichiometric ratio, leading to further burn-off and release of more CO and CO₂, which can subsequently leave the PC with lower oxygen content and vice versa [50].

Table 1. Elemental composition of porous carbons derived from KOH-neutralised BCA precursors.

Precursor	Pyrolysed Product	Elemental composition (wt%)			O/C molar ratio (from EA)	O/C molar ratio (from XPS) ^a
		C	H	O		
	P-K2-TP	79.79	1.64	18.50	0.175	0.313
	P-K3-TM	84.35	1.63	14.02	0.125	0.120
	P-K4-PM	87.72	1.05	11.22	0.096	0.277
	P-K6-M	91.20	0.83	7.97	0.066	0.258

^a Derived from the atomic percentages reported in Table S1

The XPS analysis of the samples shows that both carbon and oxygen are present, while no evidence of residual potassium is seen (Fig. 2 and Tables S1-2, see SI). The C 1s spectrum consists of five peaks including pure carbon and oxidised carbon. All spectra are similar, which is expected for this group of samples as the only difference between them is the number of oxidised carbons on the precursor material. As observed by Raman spectroscopy (Fig. S3, see SI), the carbon-carbon bonds are present as a mixture of sp^2 and sp^3 hybridisations, displaying binding energies of 284.5 and 284.8 eV, respectively. The oxidised carbon is a mixture of alcohols/ethers (286.1-286.5 eV), carbonyls (287.4-287.9 eV) and carboxylate-like groups (288.6-288.9 eV) [44, 46, 47, 51]. However, it is only by correlating the C 1s data with the O 1s data that the true nature of the carbon-oxygen bonds can be elucidated. Deconvolution of the O 1s spectra reveals three main contributions, whose binding energies suggest presence of C=O (531.4 eV), C-O (533.0 eV) and O-H groups (534.0 eV) [44, 46, 47, 51]. Except for P-K3-TM, the ratios of carbon to oxygen in the samples are not in good agreement with those obtained by elemental analysis (Table 1). However, it is important to note here that XPS is a surface technique and only scans the top 5 nm of a sample, whereas elemental analysis is a bulk technique. In addition, elemental analysis measures the quantity of hydrogen present in the sample, which XPS is unable to do. Comparing the values of CHN analysis and XPS, we can see that P-K4-PM and P-K6-M have most of their oxygen concentrated near the external surface. A similar observation can be made for P-K2-TP, even though in this case the discrepancy between CHN and XPS is smaller.

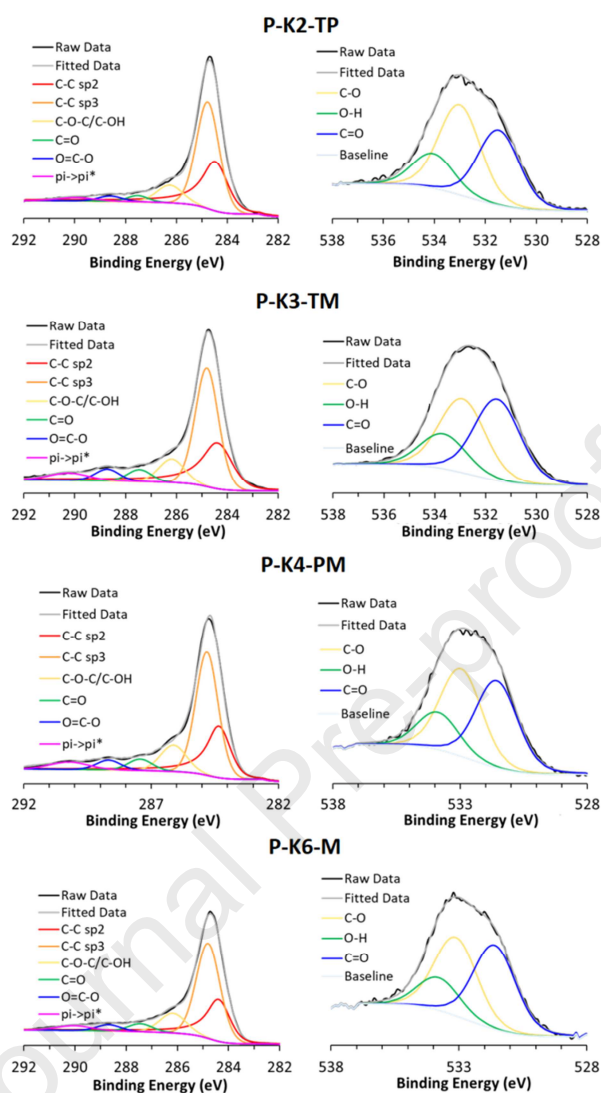


Fig. 2 XPS spectra of the samples P-K2-TP, P-K3-TM, P-K4-PM and P-K6-M. High resolution spectra of C 1s (left) and O 1s (right).

N_2 sorption analysis at 77 K reveals that all the samples are predominantly microporous, adsorbing most N_2 at P/P_0 below 0.1. P-K4-PM and P-K6-M also feature little hysteresis above 0.4 P/P_0 , suggesting that they contain a small amount of mesopores (Fig. 3a). BET surface areas range between $1210 \text{ m}^2 \text{ g}^{-1}$ for P-K2-TP and $1933 \text{ m}^2 \text{ g}^{-1}$ for P-K6-M (Table 2). The total pore volume increases with increasing number of carboxylic groups in the precursor, but in terms of micropore volume P-K3-TM is higher than P-K4-PM ($0.57 \text{ cm}^3 \text{ g}^{-1}$ vs $0.49 \text{ cm}^3 \text{ g}^{-1}$, respectively, Table 2). The pore size distribution (PSD) derived from the N_2 isotherms at 77 K shows that P-K6-M features a much larger share of supermicropores having diameter comprised between 1 and 2 nm than the other samples (Fig. 3b and Fig. S4

see SI). These pores make up nearly 50% of the pore volume of P-K6-M. CO₂ sorption analysis at 273 K reveals that P-K3-TM uptakes a remarkable 150 cm³ g⁻¹ (6.7 mmol g⁻¹) at 760 torr, with the other samples all reaching values in the vicinity of 120 cm³ g⁻¹ (5.4 mmol g⁻¹) (Fig. 3c). PSD derived from the CO₂ isotherms at 273 K displays similar pore structure, with P-K3-TM having the highest share of ultramicropores (i.e. with diameter < 8 Å), peaking at 0.32 cm³ g⁻¹ (Fig. 3d and Fig. S5). P-K6-M displays the lowest amount of very narrow pores having diameter between 3 and 4 Å, which can be especially effective for CO₂ adsorption at low pressure.

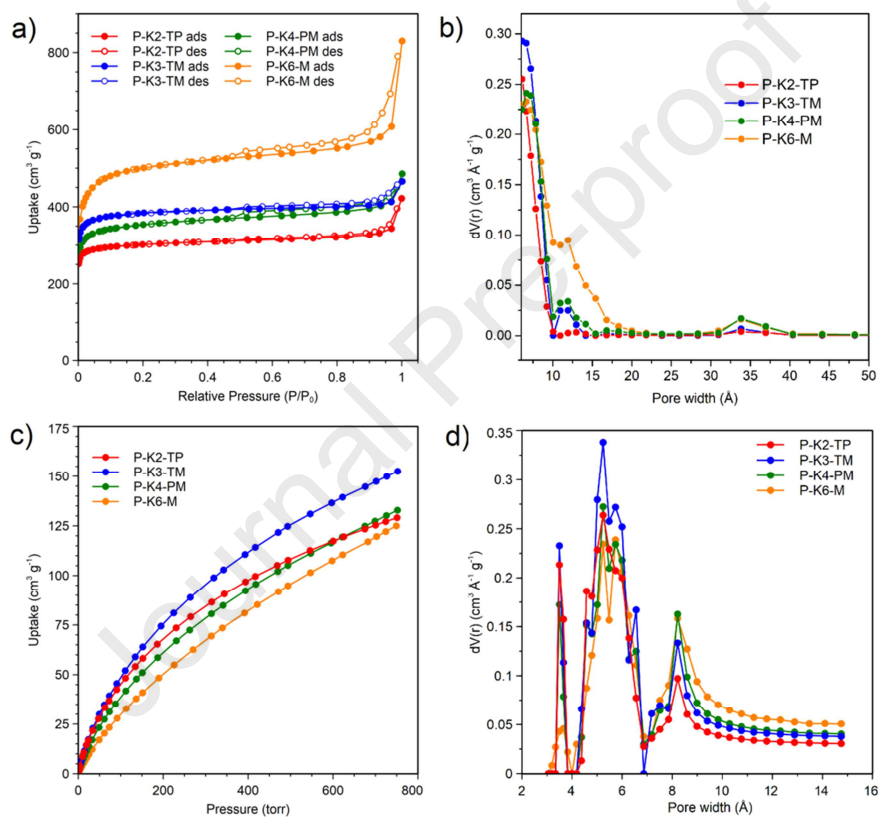


Fig. 3 N₂ adsorption isotherms collected at 77 K (a) and resulting pore size distribution (b), CO₂ adsorption isotherms collected at 273 K up to 760 torr (c) and resulting pore size distribution (d) for P-K2-TP (red), P-K3-TM (blue), P-K4-PM (olive) and P-K6-M (orange). Displayed lines connect experimental points.

Table 2. Textural properties and CO₂ uptake values at various pressures for P-K2-TP, P-K3-TM, P-K4-PM and P-K6-M.

Sample	BET s.a. (m ² g ⁻¹)	Total pore volume ^a (cm ³ g ⁻¹)	Micropore volume ^b (cm ³ g ⁻¹)	Ultramicropore volume ^c (cm ³ g ⁻¹)	CO ₂ uptake at 25 °C ^d (mmol g ⁻¹)		
					0.15 bar	1 bar	10 bar
P-K2-TP	1210	0.51	0.44	0.27	1.3	4.0	8.2
P-K3-TM	1533	0.63	0.57	0.32	1.3	4.4	10.1
P-K4-PM	1390	0.64	0.49	0.26	1.1	3.9	9.5
P-K6-M	1933	0.88	0.69	0.24	0.9	3.8	12.4

^a Measured at $P/P_0 = 0.9$; ^b From t-plot applied to N₂ isotherm; ^c Cumulative pore volume at pore width of 8 Å from pore size distribution derived from CO₂ sorption at 273 K (Figure S5); ^d From high pressure CO₂ isotherms.

High pressure CO₂ isotherms, measured up to 10 bar at 25 °C, show that P-K3-TM perform best at pressure below 1 bar, up-taking as much as 4.4 mmol g⁻¹ of CO₂, but P-K6-M is able to adsorb considerably more CO₂ than any other sample at 10 bar (12.4 mmol g⁻¹) (Fig. 4a and Table 2). These observations can be rationalised by noting that P-K3-TM has the largest amount of ultra-micropores, which are effective in adsorbing CO₂ at low pressure, whereas P-K6-M has the largest amount of large micropores, which require higher pressures to be covered. The different behaviour of P-K2-TP and P-K4-PM at low pressure could be explained invoking two concurring factors: the samples have similar ultra-micropore volume (0.27 cm³ g⁻¹ vs 0.26 cm³ g⁻¹, respectively, Table 2), even though P-K2-TP displays slightly higher cumulative pore volume below 5 Å (Fig. S5); in addition, P-K2-TP contains nearly twice as much oxygen than P-K4-PM (18.50% vs 11.22%, respectively), which could be beneficial to further increase the affinity of its surface for CO₂. The remarkable performance displayed by P-K3-TM at low pressure can be attributed to a favourable combination of high ultra-micropore volume and oxygen content (14.02%). This is in line with some very recent works, which suggest that both narrow micropores and oxygenated functional groups are indeed necessary to increase the affinity for CO₂ [46, 47]. This is likely due to the polar character conferred to small pores by oxygenated functionalities, where the adsorbate experiences intimate interactions with the pore walls, thus creating a favourable environment for the strongly quadrupolar and highly polarisable CO₂ molecule. The fact that P-K3-TM (ultra-micropore volume = 0.32 cm³ g⁻¹, oxygen content = 14.02%) performs slightly better than P-K2-TP (ultra-micropore volume = 0.27 cm³ g⁻¹, oxygen content = 18.50%) at 0.15 bar points towards ultra-micropore volume being more important than oxygen content. In order to gain more insight into the adsorption behaviour of the samples, the isosteric heat of CO₂

adsorption (Q_{st}) was extracted from the CO_2 adsorption isotherms collected at 25, 35 and 45 °C, which were fitted with both the Dual Site Langmuir equation, applying the Clausius-Clapeyron equation, and the Virial equation (Fig. S6-13, Tables S3-10). The trends of Q_{st} derived from the Clausius-Clapeyron equation suggest that P-K2-TP and P-K3-TM could reach higher values than the other samples, but the fact that these grow as the loading increased up to about 2 mmol g^{-1} indicates that the model does not provide a completely realistic picture of the phenomenon, because the strongest adsorption sites (i.e. those with higher Q_{st}) should be filled first and the Q_{st} should gradually decrease at higher loadings (Fig. S14). The Q_{st} trends obtained from the Virial equation are, instead, more canonical (Fig. 4c) and appear to confirm the beneficial effect of oxygen content: P-K2-TP and P-K3-TM display Q_{st} at zero coverage of 31 and 30 kJ mol^{-1} , respectively, more than 2 kJ mol^{-1} larger than that of P-K4-PM and more than 4 kJ mol^{-1} larger than that of P-K6-M. High pressure N_2 isotherms, measured up to 10 bar at 25 °C, show that P-K3-TM uptakes the least amount of N_2 , whereas the other samples show very similar trends (Fig. 4b, Fig. S15-18, Tables S11-14). This suggests that the combination of large ultra-micropore volume and high oxygen content is beneficial in reducing the affinity for N_2 . This is in stark contrast with what observed for CO_2 and can be rationalised based on the small quadrupolar moment and polarisability of the N_2 molecule. The combination of high CO_2 and low N_2 uptake makes P-K3-TM remarkably more selective than the other samples. The calculated CO_2/N_2 selectivity of P-K3-TM, according to the ideal adsorbed solution theory (IAST) for a 0.15:0.85 mixture at 1 bar total pressure, is 32, about twice as much as that displayed by the other samples (comprised between 12 for P-K6-M and 18 for P-K2-TP, Fig. 4d). Furthermore, the selectivity of P-K3-TM increases with pressure, reaching a value of 55 at a total pressure of 10 bar, whereas the other samples stay roughly constant in the same pressure range. The combination of high CO_2 uptake and high selectivity makes P-K3-TM a promising sorbent for application in a pressure swing adsorption separation process. When compared with other PCs reported in the literature, P-K3-TM displays CO_2 uptake, at both 0.15 bar and 1 bar at 25 °C, competitive with the best performing sorbents (Table S15). It is worth to note that all methods used to prepare PCs in Table S15 (see SI) rely on the alkali-metal activation through changing the ratio between precursor and activator and there is no stoichiometric-based calculation.

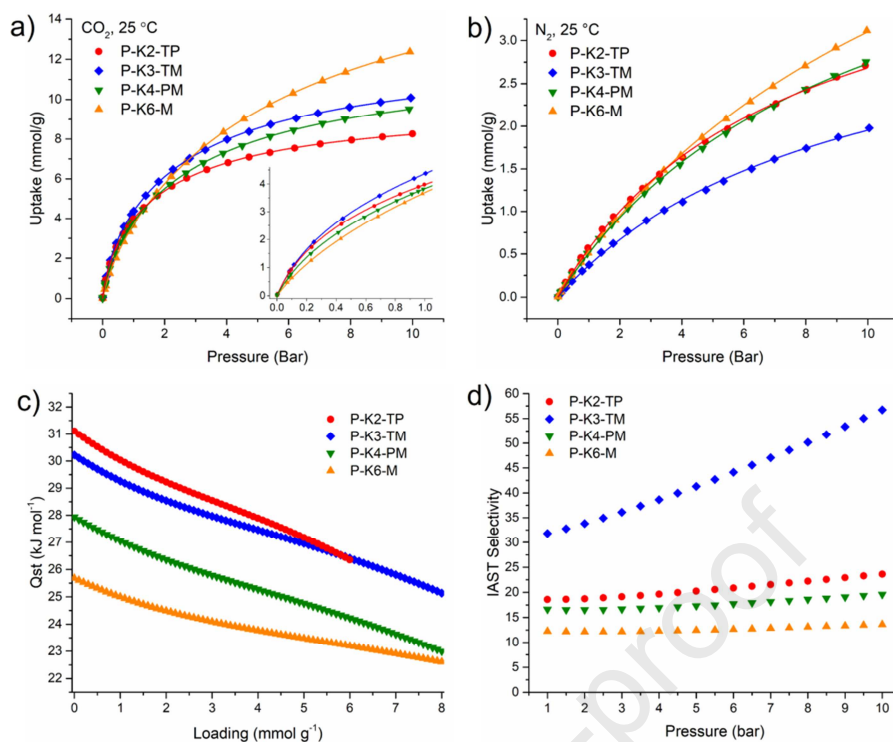


Fig. 4 High pressure CO_2 adsorption isotherms (with inset up to 1 bar) collected at 25 °C (a), high pressure N_2 adsorption isotherms collected at 25 °C (b), isosteric heats of CO_2 adsorption (Q_{st} , c) derived from Virial fitting and IAST selectivity in the 1-10 bar pressure range at 25 °C for a 0.15:0.85 CO_2/N_2 mixture (d) for P-K2-TP (red), P-K3-TM (blue), P-K4-PM (olive) and P-K6-M (orange). Displayed lines are Dual Site Langmuir fits in (a) and Langmuir fits in (b).

Effect of the charge balancing species

Having observed that H3-TM could be pyrolysed with no need to neutralise with KOH, we sought to gain better understanding of the trimesate precursor system by investigating the properties of porous carbons derived from the same carboxylate species, but with different charge balancing species, i.e. H, Na and K.

As can be seen from Fig. 5, the morphology of the three samples varies considerably: oval shaped particles with size < 100 nm are seen for P-H3-TM, P-Na3-TM takes the shape of vesicular particles, while P-K3-TM led to spherical particles, as already noted above. SEM and TEM figures are displayed in Fig. S19-20 (see SI).

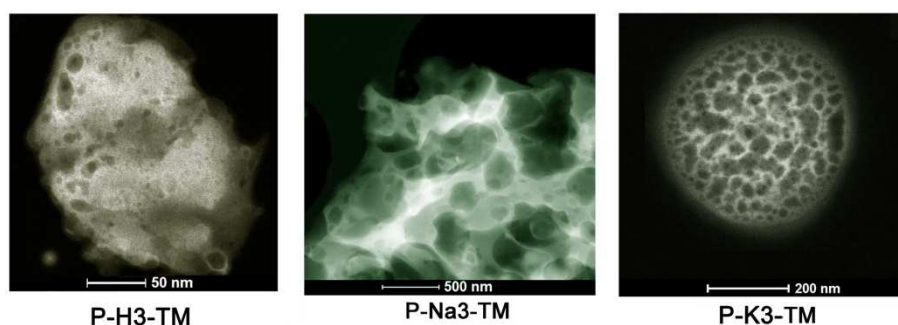
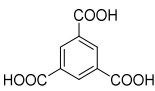
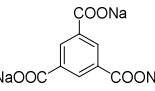
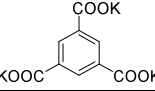


Figure 5. STEM images of PH-3-TM, P-Na3TM, and P-K3-TM.

CHN elemental analysis shows that the oxygen content found in the pyrolysed product is influenced by the nature of the cationic species and it increases in the order $H < Na \ll K$ (Table 3). This trend might be related with different interactions between the carboxylate groups and the positive species existing in the precursors, which become stronger as the size of the cation becomes larger, thus leading to retaining more oxygen upon pyrolysis. We are not aware of other studies employing similar precursors, therefore there is no reliable term of comparison against which our results can be benchmarked.

Table 3. Elemental composition of porous carbons derived from trimesate precursors with different charge balancing species.

Precursor	Pyrolysed Product	Elemental composition (wt%)			O/C molar ratio (from EA)	O/C molar ratio (from XPS)
		C	H	O		
	P-H3-TM	97.00	0.21	2.79	0.021	0.233
	P-Na3-TM	93.23	0.67	6.10	0.049	0.083
	P-K3-TM	84.35	1.63	14.02	0.125	0.120

The XPS spectra were fit and peaks assigned following the method described in the previous section (Fig. 6). For all samples the ratio between sp^2 and sp^3 carbon is in favour of the former. However, in going from P-H3-TM to P-Na3-TM to P-K3-TM the ratio decreases (Table S16). Although this dominance is not observed in the Raman spectroscopy (Fig. S21, see SI), where all the spectra are very similar, this is probably due to the high surface sensitivity achieved using XPS. From the O 1s spectra, the same three oxygen environments are observed, with no outstanding differences between different samples. It is worth noting

that P-H3-TM has the lowest O/C ratio from CHN analysis (0.021), but the highest one (0.233) from XPS, suggesting that majority of the oxygen is concentrated near its external surface (Table 3).

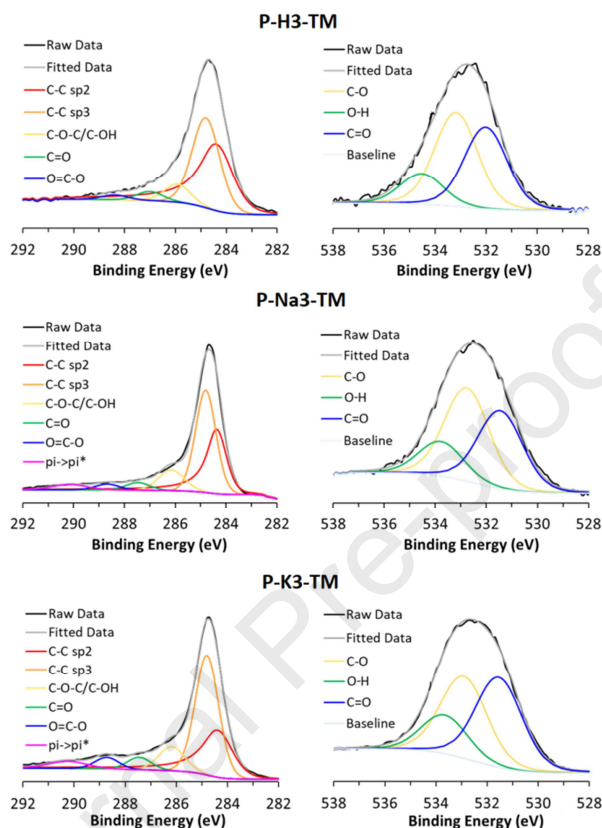


Fig. 6 XPS spectra of the samples P-H3-TM, P-Na3-TM and P-K3-TM. High resolution spectra of (left) C 1s and (right) O 1s.

N_2 sorption analysis at 77 K reveals that P-H3-TM and P-Na3-TM have very similar isotherms, leading to determine BET surface areas of $681 \text{ m}^2 \text{ g}^{-1}$ and $708 \text{ m}^2 \text{ g}^{-1}$, respectively, much lower than that of P-K3-TM ($1533 \text{ m}^2 \text{ g}^{-1}$, Fig. 7a and Table 4). The same trend can be seen for total pore volume, micropore volume and ultra-micropore volume (Table 4). Accordingly, the pore size distribution (PSD) derived from the N_2 isotherms at 77 K shows that P-K3-TM features a larger share of large micropores than P-H3-TM and P-Na3-TM (Fig. 7b and Figure S22). The lower porosity of P-H3-TM and P-Na3-TM is indicative of less burn-off occurring during pyrolysis. CO_2 sorption analysis at 273 K reveals that P-H3-TM and P-Na3-TM uptake considerably less CO_2 than P-K3-TM at 760 torr ($90 \text{ cm}^3 \text{ g}^{-1}$ or 4.0 mmol g^{-1} for P-H3-TM; $113 \text{ cm}^3 \text{ g}^{-1}$ or 5.0 mmol g^{-1} for P-Na3-TM; $150 \text{ cm}^3 \text{ g}^{-1}$ or 6.7 mmol g^{-1} for P-K3-TM; Fig. 7c). PSD derived from the CO_2 isotherms at 273 K displays similar

pore structure, with P-K3-TM having a much larger share of ultra-micropores than the other two samples (Fig. 7d and Fig. S23 see SI).

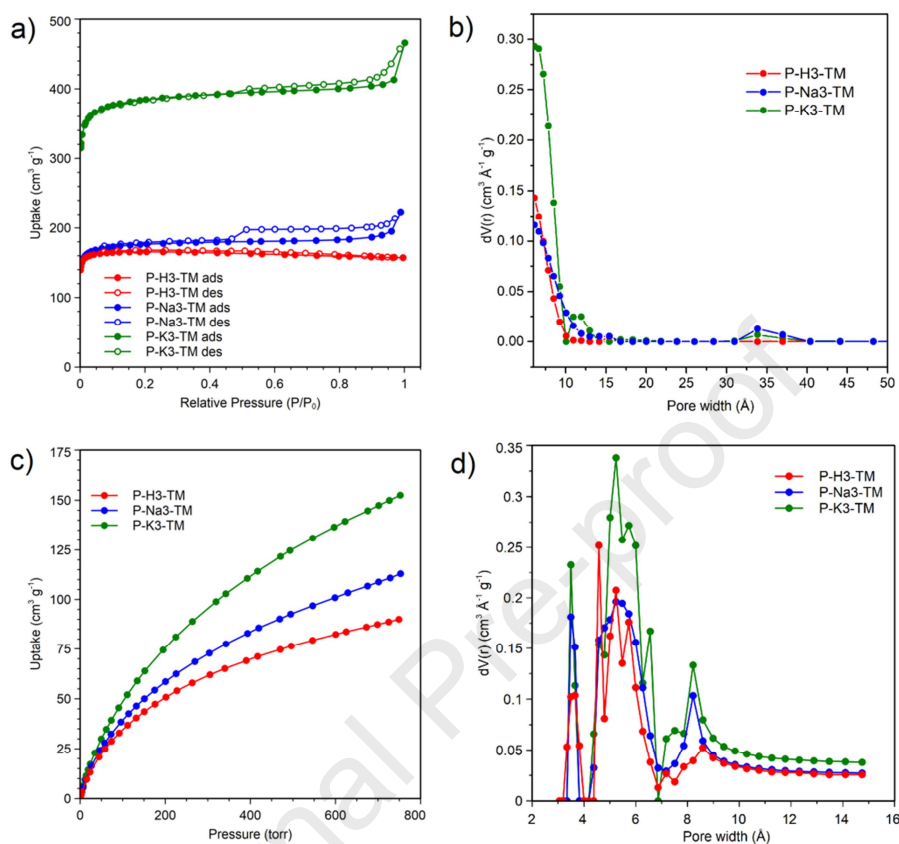


Fig. 7 N₂ adsorption isotherms collected at 77 K (a) and resulting pore size distribution (b), CO₂ adsorption isotherms collected at 273 K up to 760 torr (c) and resulting pore size distribution (d) for P-H3-TM (red), P-Na3-TM (blue) and P-K3-TM (olive). Displayed lines connect experimental points.

Table 4. Textural properties and CO₂ uptake values at various pressures for P-H3-TM, P-Na3-TM and P-K3-TM.

Sample	BET s.a. (m ² g ⁻¹)	Total pore volume ^a (cm ³ g ⁻¹)	Micropore volume ^b (cm ³ g ⁻¹)	Ultramicropore volume ^c (cm ³ g ⁻¹)	CO ₂ uptake at 25 °C ^d (mmol g ⁻¹)		
					0.15 bar	1 bar	10 bar
P-H3-TM	681	0.25	0.25	0.19	1.1	3.0	5.6
P-Na3-TM	708	0.31	0.26	0.23	1.2	3.3	6.5
P-K3-TM	1533	0.63	0.57	0.32	1.3	4.4	10.1

^a Measured at P/P₀ = 0.9; ^b From t-plot applied to N₂ isotherm; ^c Cumulative pore volume at pore width of 8 Å from pore size distribution derived from CO₂ sorption at 273 K (Figure S18); ^d From high pressure CO₂ isotherms.

High pressure CO₂ isotherms, measured up to 10 bar at 25 °C, show that P-K3-TM performs best over the whole pressure range (Fig. 8a and Table 4). This is due to the fact that P-K3-TM has the largest volume of micropores and ultra-micropores and the highest oxygen content of the series. The trends of Q_{st} show that P-H3-TM has the highest value at zero coverage (32.5 kJ mol⁻¹), exceeding those of P-Na3-TM and P-K3-TM, both displaying 30 kJ mol⁻¹ (Fig. 8c, Fig. S24-28, Tables S17-20). This observation is not straightforward to rationalise, as P-H3-TM has both the lowest oxygen content and the lowest ultra-micropore volume. A possible explanation is that this sample features peculiar surface chemistry within the bulk that enhances the affinity for CO₂ and escapes the range probed by XPS. High pressure N₂ isotherms show that P-K3-TM uptakes the least amount of N₂, whereas the other samples show very similar trends (Fig. 8b). This further confirms that a combination of ultra-micropores and high oxygen content is crucial to reduce the affinity to N₂. Also in this case, the calculated CO₂/N₂ selectivity at 1 bar total pressure of P-K3-TM (32) is much higher than that displayed by the other samples in the same conditions (20) (Fig. 8d, Fig. S29-30, Tables S21-22 see SI). These results suggest that neutralisation with KOH is essential to produce a PC with a combination of high micropore volume and oxygen content, which performs much better than the products obtained from either direct pyrolysis of the polyacid precursor or pyrolysis of a NaOH neutralised precursor.

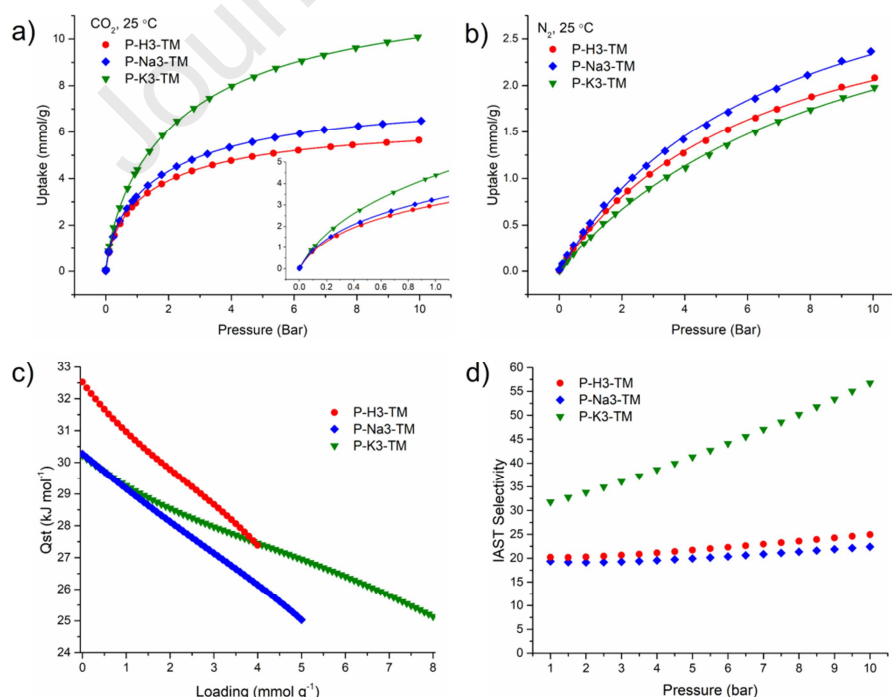


Fig. 8 High pressure CO₂ adsorption isotherms (with inset up to 1 bar) collected at 25 °C (a), high pressure N₂ adsorption isotherms collected at 25 °C (b), isosteric heats of CO₂

adsorption (Qst, c) derived from Virial fitting and IAST selectivity in the 1-10 bar pressure range at 25 °C for a 0.15:0.85 CO₂/N₂ mixture (d) for P-H3-TM (red), P-Na3-TM (blue) and P-K3-TM (olive). Displayed lines are Dual Site Langmuir fits in (a) and Langmuir fits in (b).

Effect of the degree of deprotonation

We found that also H6-M could be pyrolysed with no need to neutralise with KOH, which suggested that we could look at the effect of a different degree of deprotonation for the mellitic precursor. Therefore, we prepared one sample starting from a half deprotonated mellitic acid precursor, named P-H3K3-TM.

A notable feature that emerges from STEM analysis is that, while P-H6-M and P-K6-M resulted in elliptical and spherical particles of similar size (about 50 nm), partial deprotonation, resulting in P-H3K3-M, yielded ultrafine and transparent carbon sheets (Fig. 9). SEM and TEM images for all samples can be found in Fig. S31-32 (see SI).

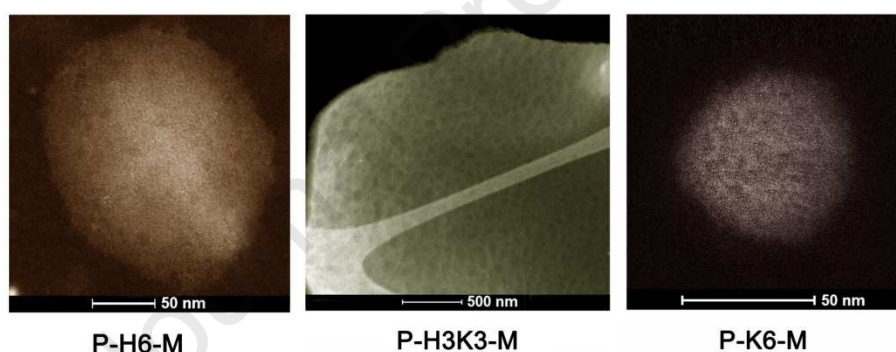
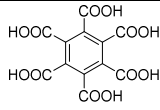
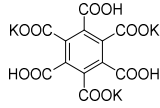
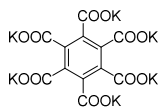


Fig. 9 STEM images of P-H6-M, P-HK3-M, P-K6-M.

CHN elemental analysis shows that the oxygen content found in the pyrolysed products depends on the degree of deprotonation and increases in the order K6 < H3K3 << H6 (Table 5). Thus, there is an evident difference between the retention of oxygen of TM and M precursors: while H3-TM retains much less oxygen than K3-TM, H6-M retains much more oxygen than K6-M. A notable difference between TM and M precursors is in the relative position of carboxylate groups: in TM, the three carboxylates are in *meta* position with respect to each other, whereas in M the six carboxylates are in *ortho* position with respect to each other. In the latter case, high temperature treatment can lead to condensation of adjacent carboxylates to form anhydrides, which are likely to stabilise the system, leading to higher oxygen retention during pyrolysis. When half of the carboxylates in M are deprotonated,

there is no possibility anymore for anhydrides to form, with consequent loss of most of the oxygen during pyrolysis. A similar explanation can be extended to the fully deprotonated mellitate precursor. XPS (Fig. 10) shows that, with increasing deprotonation, the oxygen tends to be more concentrated on the external surface (Table 5 and Table S23 see SI). Whilst the spectra of the deprotonated materials are similar to those discussed earlier in the manuscript, there are some differences for P-H3K3-M: this sample does not display the O-H feature in the O 1s spectrum. P-H6-M also differs in that there is no contribution to the C 1s spectrum from pi-pi* interactions. Raman spectra display very similar G-D ratio for all samples (Fig. S33, see SI).

Table 5. Elemental composition of porous carbons derived from mellitate precursors at different deprotonation degrees.

Precursor	Pyrolysed Product	Elemental analysis (wt%)			O/C molar ratio (from EA)	O/C molar ratio (from XPS)
		C	H	O		
	P-H6-M	66.32	0.64	33.04	0.375	0.110
	P-H3K3-M	89.88	0.88	9.24	0.077	0.131
	P-K6-M	91.20	0.83	7.97	0.066	0.258

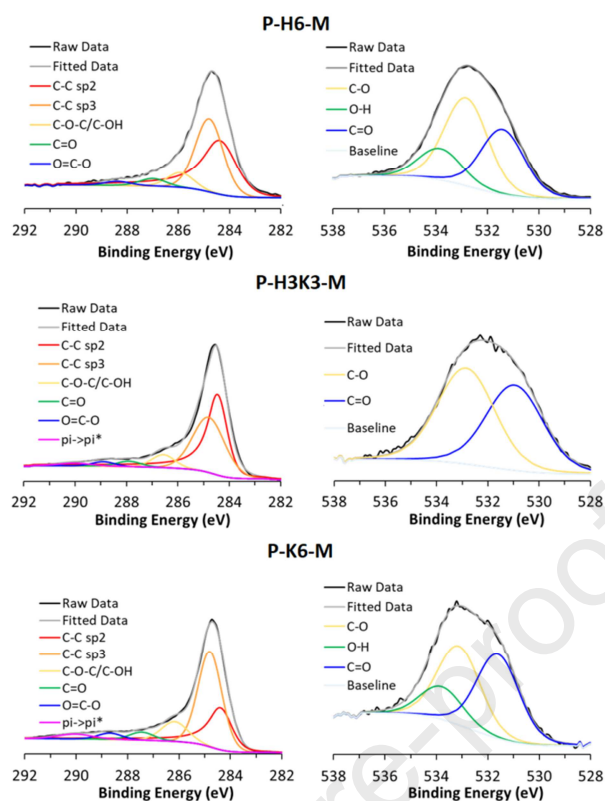


Fig. 10 XPS spectra of the samples P-H6-M, P-H3K3-TM and P-K6-M. High resolution spectra of (left) C 1s and (right) O 1s.

N_2 sorption analysis at 77 K reveals that P-H6-M and P-H3K3-M also display isotherms indicative of abundant microporosity, but their N_2 uptake at saturation is considerably different, leading to determine BET surface areas of $1214 \text{ m}^2 \text{ g}^{-1}$ and $2252 \text{ m}^2 \text{ g}^{-1}$, respectively (Fig. 11a and Table 6). Both these values are, in turn, quite different from that of P-K6-M ($1933 \text{ m}^2 \text{ g}^{-1}$, Fig. 11a and Table 6). The same trend can be seen for total pore volume, micropore volume and ultra-micropore volume (Table 6). The pore size distribution (PSD) derived from the N_2 isotherms at 77 K shows that P-H3K3-M and P-K6-M feature a similarly large share of large micropores, much larger than P-H6-M, (Fig. 11b and Fig. S34 see SI). CO_2 sorption analysis at 273 K reveals that P-H3K3-M is able to uptake more CO_2 than the other samples at 760 torr ($163 \text{ cm}^3 \text{ g}^{-1}$ or 7.3 mmol g^{-1} for P-H3K3-M; about $126 \text{ cm}^3 \text{ g}^{-1}$ or 5.6 mmol g^{-1} for P-H6-M and P-K6-M; Fig. 11c). PSD derived from the CO_2 isotherms at 273 K displays similar pore structure, with P-H3K3-M having a much larger share of ultra-micropores than the other two samples (Fig. 11d and Fig. S27, see SI).

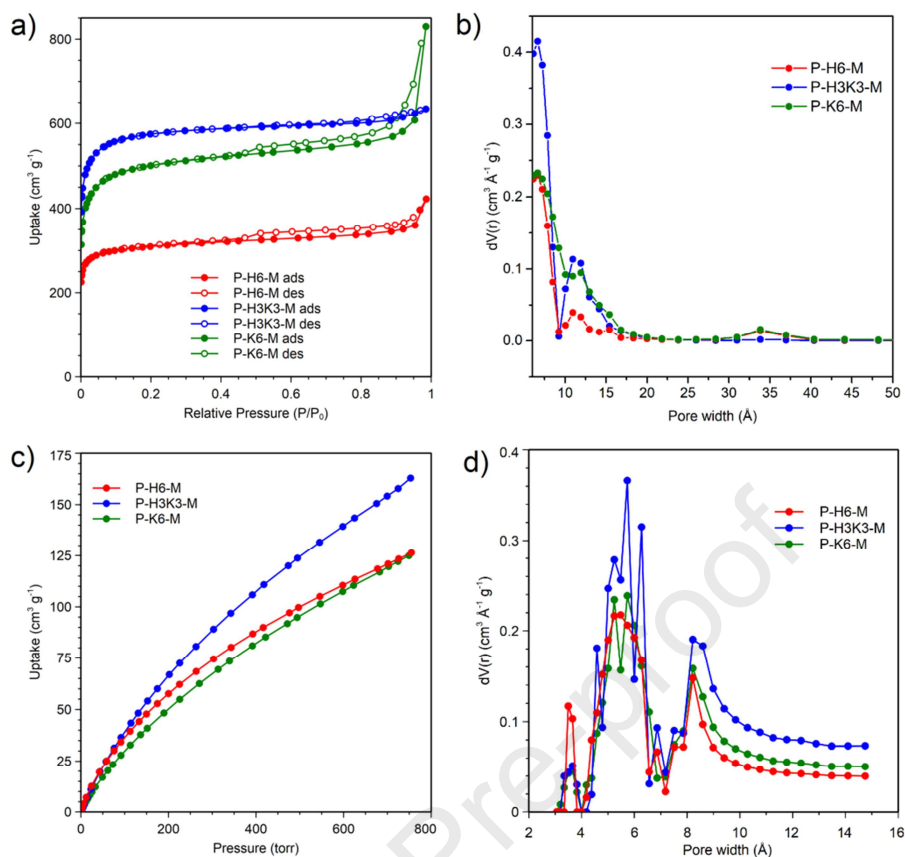


Fig. 11 N₂ adsorption isotherms collected at 77 K (a) and resulting pore size distribution (b), CO₂ adsorption isotherms collected at 273 K up to 760 torr (c) and resulting pore size distribution (d) for P-H6-M (red), P-H3K3-M (blue) and P-K6-M (olive). Displayed lines connect experimental points.

Table 6. Textural properties and CO₂ uptake values at various pressures for P-H6-M, P-H3K3-M and P-K6-M.

Sample	BET s.a. (m ² g ⁻¹)	Total pore volume ^a (cm ³ g ⁻¹)	Micropore volume ^b (cm ³ g ⁻¹)	Ultramicropore volume ^c (cm ³ g ⁻¹)	CO ₂ uptake at 25 °C ^d (mmol g ⁻¹)		
					0.15 bar	1 bar	10 bar
P-H6-M	1214	0.54	0.43	0.25	1.4	4.2	8.4
P-H3K3-M	2252	0.94	0.85	0.31	1.0	4.0	12.2
P-K6-M	1933	0.88	0.69	0.24	0.9	3.8	12.4

^a Measured at $P/P_0 = 0.9$; ^b From t-plot applied to N₂ isotherm; ^c Cumulative pore volume at pore width of 8 Å from pore size distribution derived from CO₂ sorption at 273 K (Figure S27); ^d From high pressure CO₂ isotherms.

High pressure CO₂ isotherms, measured up to 10 bar at 25 °C, show that P-H6-M performs best in the pressure range below 1 bar (Fig. 12a and Table 6). P-K6-M and P-H3K3-M display similar trends, with the latter performing slightly better at low pressure. We

attribute this to the fact that P-H6-M has by far the largest oxygen content (33.04%) of the series, most of which is concentrated in the bulk and probably compensates its relatively low ultra-micropore volume. This is corroborated by the value of Q_{st} for this sample, which tops at 32 kJ mol^{-1} at zero coverage, 6 kJ mol^{-1} higher than P-K6-M and P-H3K3-M (Fig. 12c, Fig. S36-40, Tables S24-27 see SI). High pressure N_2 isotherms show that all the samples uptake similar amounts of N_2 (Fig. 12b, Fig. S41-42, Tables S28-S29 see SI). Thanks to the higher CO_2 uptake at low pressure, the calculated CO_2/N_2 selectivity of P-H6-M at 1 bar total pressure (18) is 50% higher than that displayed by the other samples (12) (Fig. 12d). These results suggest that a high oxygen content in PCs is mainly beneficial at low partial pressures, affording improved uptake and selectivity. Partial neutralisation of the precursor affords a different product from full neutralisation in terms of textural properties, but with similar oxygen content, even though the distribution of this oxygen within the sorbent changes. However, in terms of CO_2 capture performance the main differences are seen when moving from the product of direct pyrolysis of the polyacid precursor to those obtained by pyrolysis of activated precursors.

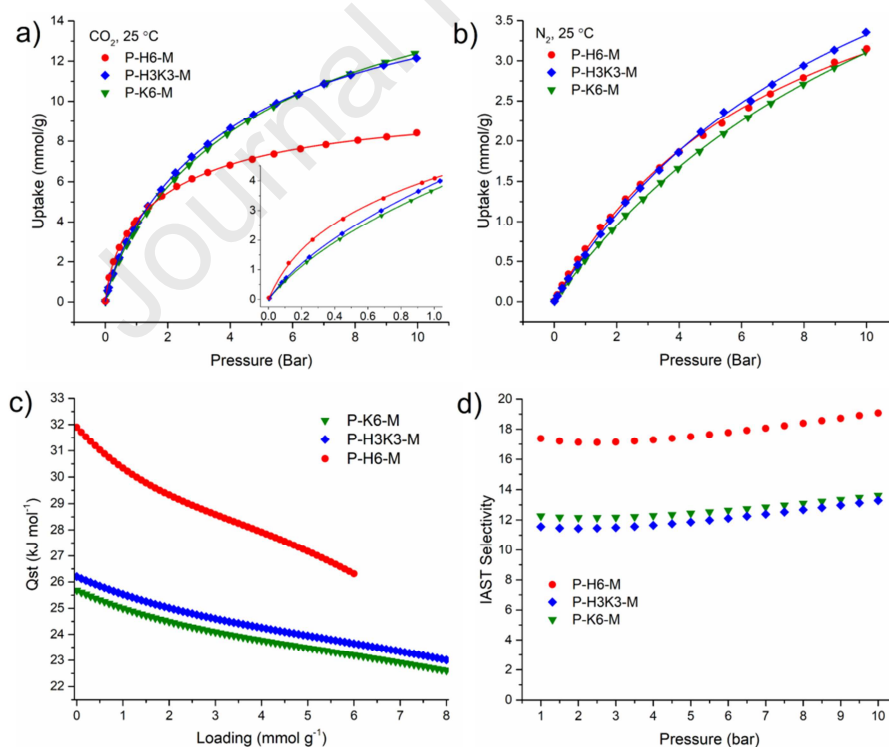


Fig. 12 High pressure CO_2 adsorption isotherms (with inset up to 1 bar) collected at 25 °C (a), high pressure N_2 adsorption isotherms collected at 25 °C (b), isosteric heats of CO_2 adsorption (Q_{st} , c) derived from Virial fitting and IAST selectivity in the 1-10 bar pressure

range for a 0.15:0.85 CO₂/N₂ mixture (d) for P-H6-M (red), P-H3K3-M (blue) and P-K6-M (olive). Displayed lines are Dual Site Langmuir fits in (a) and Langmuir fits in (b).

Conclusion

In this work, we studied the morphology, chemical composition, textural properties and CO₂/N₂ separation performance of PCs obtained by pyrolysis of benzene polycarboxylate precursors. Carboxylic groups provide an opportunity to produce oxygen doped PCs by employing stoichiometric amounts of hazardous alkali metal based activating agents. In all cases, PCs with high share of micropores were obtained, whereas ultra-microporosity and oxygen content proved to be dependent on the nature of the precursor. Systematic investigation of three parameters was undertaken to understand their effect on the properties of the resulting PCs: (i) number of carboxylate groups in the KOH neutralised precursor, ranging from two to six; (ii) nature of the charge balancing species in a trimesate precursor, namely H, Na and K; (iii) degree of deprotonation in a mellitate precursor. We found that increasing the number of carboxylic groups - and therefore the amount of K - in the precursor led to decreasing oxygen content and ultra-microporosity, accompanied by lower uptake of CO₂ at low pressure and CO₂/N₂ selectivity. Changing the cation in the trimesate precursor showed that K⁺ affords a PC with higher oxygen content and ultra-microporosity (P-K3-TM), resulting in better separation performance, than H⁺ and Na⁺. The main effect of the degree of deprotonation was observed when moving from a fully protonated mellitate (P-H6-M) to a half deprotonated one (P-H3K3-M). Overall, the best performance, in terms of both CO₂ uptake at 0.15 and 1 bar and CO₂/N₂ selectivity, was observed for P-K3-TM, which features the third highest oxygen content and highest ultra-micropore volume of all the investigated samples. High oxygen content (as exemplified by P-H6-M) or high ultramicroporosity (as exemplified by P-H3K3-M) alone were not enough to boost both CO₂ uptake and CO₂/N₂ selectivity. This indicates that the interplay between ultra-microporosity and oxygen content matters more than the two features taken singularly. P-K3-TM shows competitive performance with other PCs reported in the literature and activated using excess of alkali metal based activating agents. Moreover, it displays a singular increase in CO₂/N₂ selectivity with increasing pressure, reaching a maximum of 55 at 10 bar, which makes it an attractive sorbent for PSA.

Acknowledgements

S. K. and M. T. wish to acknowledge funding from the European Union's Horizon 2020 research and innovation programme under the Marie Skłodowska-Curie grant agreement No 663830. Financial support was also provided by the Reduce Industrial Carbon Emissions (RICE) and Flexible Integrated Energy Systems (FLEXIS) research operations part funded by the EU's European Regional Development Fund through the Welsh Government. The authors would also like to acknowledge the assistance provided by the Swansea University AIM Facility, which was funded in part by the EPSRC (EP/M028267/1), the European Regional Development Fund through the Welsh Government (80708) and the Sêr Solar project via the Welsh Government.

Journal Pre-proof

References

- [1] G. Magnabosco, I. Papiano, M. Aizenberg, J. Aizenberg, G. Falini, Beyond biotemplating: multiscale porous inorganic materials with high catalytic efficiency, *Chemical Communications* 56(23) (2020) 3389-3392.
- [2] H. Zheng, F. Gao, V. Valtchev, Nanosized inorganic porous materials: fabrication, modification and application, *Journal of Materials Chemistry A* 4(43) (2016) 16756-16770.
- [3] H. Wang, D. Jiang, D. Huang, G. Zeng, P. Xu, C. Lai, M. Chen, M. Cheng, C. Zhang, Z. Wang, Covalent triazine frameworks for carbon dioxide capture, *J. Mat. Chem. A* 7(40) (2019) 22848-22870.
- [4] M.R. Benzigar, S.N. Talapaneni, S. Joseph, K. Ramadass, G. Singh, J. Scaranto, U. Ravon, K. Al-Bahily, A. Vinu, Recent advances in functionalized micro and mesoporous carbon materials: synthesis and applications, *Chemical Society Reviews* 47(8) (2018) 2680-2721.
- [5] Z. Zhang, Z.P. Cano, D. Luo, H. Dou, A. Yu, Z. Chen, Rational design of tailored porous carbon-based materials for CO₂ capture, *Journal of Materials Chemistry A* 7(37) (2019) 20985-21003.
- [6] N. Hosono, A. Terashima, S. Kusaka, R. Matsuda, S. Kitagawa, Highly responsive nature of porous coordination polymer surfaces imaged by in situ atomic force microscopy, *Nature Chemistry* 11(2) (2019) 109-116.
- [7] B.R. Thompson, T.S. Horozov, S.D. Stoyanov, V.N. Paunov, Hierarchically structured composites and porous materials from soft templates: fabrication and applications, *Journal of Materials Chemistry A* 7(14) (2019) 8030-8049.
- [8] G.A. Ferrero, N. Diez, M. Sevilla, A.B. Fuertes, Iron/Nitrogen co-doped mesoporous carbon synthesized by an endo-templating approach as an efficient electrocatalyst for the oxygen reduction reaction, *Microporous and Mesoporous Materials* 278 (2019) 280-288.
- [9] Q. Wang, D. Astruc, State of the Art and Prospects in Metal–Organic Framework (MOF)-Based and MOF-Derived Nanocatalysis, *Chemical Reviews* 120(2) (2020) 1438-1511.
- [10] E. Fernandez-Bartolome, J. Santos, S. Khodabakhshi, L.J. McCormick, S.J. Teat, C.S. de Pípaon, J.R. Galan-Mascarós, N. Martín, J. Sanchez Costa, A robust and unique iron(ii) mosaic-like MOF, *Chemical Communications* 54(44) (2018) 5526-5529.
- [11] Novel porous materials for emerging applications, *Journal of Materials Chemistry* 16(7) (2006) 623-625.
- [12] M.E. Davis, Ordered porous materials for emerging applications, *Nature* 417(6891) (2002) 813-821.
- [13] K. Vasanth Kumar, F. Rodríguez-Reinoso, Effect of pore structure on the selectivity of carbon materials for the separation of CO₂/H₂ mixtures: new insights from molecular simulation, *RSC Advances* 2(25) (2012) 9671-9678.
- [14] G. Chen, S. Lu, J. Zhang, Q. Xue, T. Han, H. Xue, S. Tian, J. Li, C. Xu, M. Pervukhina, B. Clennell, Research of CO₂ and N₂ Adsorption Behavior in K-Illite Slit Pores by GCMC Method, *Scientific Reports* 6(1) (2016) 37579.
- [15] R.S. Pillai, H. Jovic, M.M. Koza, F. Nouar, C. Serre, G. Maurin, N.A. Ramsahye, Diffusion of Carbon Dioxide and Nitrogen in the Small-Pore Titanium Bis(phosphonate) Metal–Organic Framework MIL-91 (Ti): A Combination of Quasielastic Neutron Scattering Measurements and Molecular Dynamics Simulations, *ChemPhysChem* 18(19) (2017) 2739-2746.
- [16] K.C. Bedin, I.P.A.F. Souza, A.L. Cazetta, L. Spessato, A. Ronix, V.C. Almeida, CO₂-spherical activated carbon as a new adsorbent for Methylene Blue removal: Kinetic, equilibrium and thermodynamic studies, *Journal of Molecular Liquids* 269 (2018) 132-139.

- [17] A. Alonso, J. Moral-Vico, A. Abo Markeb, M. Busquets-Fité, D. Komilis, V. Puentes, A. Sánchez, X. Font, Critical review of existing nanomaterial adsorbents to capture carbon dioxide and methane, *Science of The Total Environment* 595 (2017) 51-62.
- [18] S. Khodabakhshi, S. Kiani, Y. Niu, A.O. White, W. Suwaileh, R.E. Palmer, A.R. Barron, E. Andreoli, Facile and environmentally friendly synthesis of ultramicroporous carbon spheres: A significant improvement in CVD method, *Carbon* 171 (2021) 426-436.
- [19] H. Han, Y. Noh, Y. Kim, S. Park, W. Yoon, D. Jang, S.M. Choi, W.B. Kim, Selective electrochemical CO₂ conversion to multicarbon alcohols on highly efficient N-doped porous carbon-supported Cu catalysts, *Green Chemistry* 22(1) (2020) 71-84.
- [20] J. Zhang, T. Yan, J. Fang, J. Shen, L. Shi, D. Zhang, Enhanced capacitive deionization of saline water using N-doped rod-like porous carbon derived from dual-ligand metal-organic frameworks, *Environmental Science: Nano* (2020).
- [21] L. Ma, J. Liu, S. Lv, Q. Zhou, X. Shen, S. Mo, H. Tong, Scalable one-step synthesis of N,S co-doped graphene-enhanced hierarchical porous carbon foam for high-performance solid-state supercapacitors, *Journal of Materials Chemistry A* 7(13) (2019) 7591-7603.
- [22] X. Yang, K. Li, D. Cheng, W.-L. Pang, J. Lv, X. Chen, H.-Y. Zang, X.-L. Wu, H.-Q. Tan, Y.-H. Wang, Y.-G. Li, Nitrogen-doped porous carbon: highly efficient trifunctional electrocatalyst for oxygen reversible catalysis and nitrogen reduction reaction, *Journal of Materials Chemistry A* 6(17) (2018) 7762-7769.
- [23] J.P. Paraknowitsch, A. Thomas, Doping carbons beyond nitrogen: an overview of advanced heteroatom doped carbons with boron, sulphur and phosphorus for energy applications, *Energy & Environmental Science* 6(10) (2013) 2839-2855.
- [24] B. Ashourirad, P. Arab, T. Islamoglu, K.A. Cychosz, M. Thommes, H.M. El-Kaderi, A cost-effective synthesis of heteroatom-doped porous carbons as efficient CO₂ sorbents, *J. Mat. Chem. A* 4(38) (2016) 14693-14702.
- [25] H. Li, J. Li, A. Thomas, Y. Liao, Ultra-High Surface Area Nitrogen-Doped Carbon Aerogels Derived From a Schiff-Base Porous Organic Polymer Aerogel for CO₂ Storage and Supercapacitors, *Adv. Funct. Mater.* 29(40) (2019) 1904785.
- [26] S. Khodabakhshi, P.F. Fulvio, E. Andreoli, Carbon black reborn: Structure and chemistry for renewable energy harnessing, *Carbon* 162 (2020) 604-649.
- [27] H. Zhu, W. Lin, Q. Li, y. Hu, s. Guo, C. Wang, F. Yan, Bipyridinium-based Ionic Covalent Triazine Frameworks for CO₂, SO₂ and NO Capture, *ACS Applied Materials & Interfaces* (2020).
- [28] M. Jahandar Lashaki, S. Khiavi, A. Sayari, Stability of amine-functionalized CO₂ adsorbents: a multifaceted puzzle, *Chemical Society Reviews* 48(12) (2019) 3320-3405.
- [29] M. Bui, C.S. Adjiman, A. Bardow, E.J. Anthony, A. Boston, S. Brown, P.S. Fennell, S. Fuss, A. Galindo, L.A. Hackett, J.P. Hallett, H.J. Herzog, G. Jackson, J. Kemper, S. Krevor, G.C. Maitland, M. Matuszewski, I.S. Metcalfe, C. Petit, G. Puxty, J. Reimer, D.M. Reiner, E.S. Rubin, S.A. Scott, N. Shah, B. Smit, J.P.M. Trusler, P. Webley, J. Wilcox, N. Mac Dowell, Carbon capture and storage (CCS): the way forward, *Energy Environ. Sci.* 11(5) (2018) 1062-1176.
- [30] H. Zhao, X. Luo, H. Zhang, N. Sun, W. Wei, Y. Sun, Carbon-based adsorbents for post-combustion capture: a review, *Greenhouse Gases: Science and Technology* 8(1) (2018) 11-36.
- [31] J. Li, X. Yan, W. Wang, Y. Zhang, J. Yin, S. Lu, F. Chen, Y. Meng, X. Zhang, X. Chen, Y. Yan, J. Zhu, Key factors controlling the gas adsorption capacity of shale: A study based on parallel experiments, *Applied Geochemistry* 58 (2015) 88-96.
- [32] B. Singh, V. Polshettiwar, Design of CO₂ sorbents using functionalized fibrous nanosilica (KCC-1): insights into the effect of the silica morphology (KCC-1 vs. MCM-41), *Journal of Materials Chemistry A* 4(18) (2016) 7005-7019.

- [33] G. Sethia, A. Sayari, Comprehensive study of ultra-microporous nitrogen-doped activated carbon for CO₂ capture, *Carbon* 93 (2015) 68-80.
- [34] S. Ghosh, M. Sevilla, A.B. Fuertes, E. Andreoli, J. Ho, A.R. Barron, Defining a performance map of porous carbon sorbents for high-pressure carbon dioxide uptake and carbon dioxide–methane selectivity, *J. Mat. Chem. A* 4(38) (2016) 14739-14751.
- [35] B. Adeniran, R. Mokaya, Is N-Doping in Porous Carbons Beneficial for CO₂ Storage? Experimental Demonstration of the Relative Effects of Pore Size and N-Doping, *Chem. Mater.* 28(3) (2016) 994-1001.
- [36] E.M. Calvo-Muñoz, F.J. García-Mateos, J.M. Rosas, J. Rodríguez-Mirasol, T. Cordero, Biomass Waste Carbon Materials as adsorbents for CO₂ Capture under Post-Combustion Conditions, *Frontiers in Materials* 3(23) (2016).
- [37] M.M. Maroto-Valer, Z. Tang, Y. Zhang, CO₂ capture by activated and impregnated anthracites, *Fuel Processing Technology* 86(14) (2005) 1487-1502.
- [38] V. Presser, J. McDonough, S.-H. Yeon, Y. Gogotsi, Effect of pore size on carbon dioxide sorption by carbide derived carbon, *Energy & Environmental Science* 4(8) (2011) 3059-3066.
- [39] Y. Jin, S.C. Hawkins, C.P. Huynh, S. Su, Carbon nanotube modified carbon composite monoliths as superior adsorbents for carbon dioxide capture, *Energy & Environmental Science* 6(9) (2013) 2591-2596.
- [40] S. Ghosh, A.R. Barron, Optimizing Carbon Dioxide Uptake and Carbon Dioxide–Methane Selectivity of Oxygen-Doped Porous Carbon Prepared from Oxygen Containing Polymer Precursors, *ChemistrySelect* 2(36) (2017) 11959-11968.
- [41] N. Sun, C. Sun, J. Liu, H. Liu, C.E. Snape, K. Li, W. Wei, Y. Sun, Surface-modified spherical activated carbon materials for pre-combustion carbon dioxide capture, *RSC Advances* 5(42) (2015) 33681-33690.
- [42] W. Xing, C. Liu, Z. Zhou, J. Zhou, G. Wang, S. Zhuo, Q. Xue, L. Song, Z. Yan, Oxygen-containing functional group-facilitated CO₂ capture by carbide-derived carbons, *Nanoscale Research Letters* 9(1) (2014) 189.
- [43] X. Song, L.a. Wang, J. Gong, X. Zhan, Y. Zeng, Exploring a New Method to Study the Effects of Surface Functional Groups on Adsorption of CO₂ and CH₄ on Activated Carbons, *Langmuir* 36(14) (2020) 3862-3870.
- [44] B. Liu, H. Li, X. Ma, R. Chen, S. Wang, L. Li, The synergistic effect of oxygen-containing functional groups on CO₂ adsorption by the glucose–potassium citrate-derived activated carbon, *RSC Advances* 8(68) (2018) 38965-38973.
- [45] Á. Sánchez-Sánchez, F. Suárez-García, A. Martínez-Alonso, J.M.D. Tascón, Influence of Porous Texture and Surface Chemistry on the CO₂ Adsorption Capacity of Porous Carbons: Acidic and Basic Site Interactions, *ACS Applied Materials & Interfaces* 6(23) (2014) 21237-21247.
- [46] X. Ma, L. Li, Z. Zeng, R. Chen, C. Wang, K. Zhou, H. Li, Experimental and theoretical demonstration of the relative effects of O-doping and N-doping in porous carbons for CO₂ capture, *Applied Surface Science* 481 (2019) 1139-1147.
- [47] X. Ma, Y. Yang, Q. Wu, B. Liu, D. Li, R. Chen, C. Wang, H. Li, Z. Zeng, L. Li, Underlying mechanism of CO₂ uptake onto biomass-based porous carbons: Do adsorbents capture CO₂ chiefly through narrow micropores?, *Fuel* 282 (2020) 118727.
- [48] A.D. Manasrah, A. Hassan, N.N. Nassar, Enhancement of petroleum coke thermal reactivity using Oxy-cracking technique, *The Canadian Journal of Chemical Engineering* 97(11) (2019) 2794-2803.
- [49] S. Lee, J.H. Lee, J. Kim, User-friendly graphical user interface software for ideal adsorbed solution theory calculations, *Korean Journal of Chemical Engineering* 35(1) (2018) 214-221.

- [50] M. Sevilla, A.B. Fuertes, R. Mokaya, High density hydrogen storage in superactivated carbons from hydrothermally carbonized renewable organic materials, *Energy & Environmental Science* 4(4) (2011) 1400-1410.
- [51] L. Balan, M.C. Fernández de Córdoba, M. Zaier, C.O. Ania, A green and fast approach to nanoporous carbons with tuned porosity: UV-assisted condensation of organic compounds at room temperature, *Carbon* 116 (2017) 264-274.

Journal Pre-proof

Declaration of interests

The authors declare that they have no known competing financial interests or personal relationships that could have appeared to influence the work reported in this paper.

The authors declare the following financial interests/personal relationships which may be considered as potential competing interests:

Journal Pre-proof